AIAA AVIATION Forum
June 27-July 1, 2022, Chicago, IL & Virtual
AIAA AVIATION 2022 Forum

10.2514/6.2022-3345

Three-Dimensional Spectral POD of Supersonic Twin-Rectangular Jet Flow

Brandon C. Y. Yeung* and Oliver T. Schmidt†
University of California San Diego, La Jolla, California 92093

Guillaume A. Brès‡
Cascade Technologies Inc., Palo Alto, California 94303

The statistical analysis of non-axisymmetric turbulent jets using spectral proper orthogonal decomposition (SPOD) is computationally costly; in particular, their non-axisymmetry precludes Fourier decomposition of the three-dimensional flow field into two-dimensional azimuthal modes. Jets in the dihedral group D_2, including rectangular, elliptic, and twin jets, are invariant under reflection about their major and minor axes. For these jets, we propose an SPOD workflow that exploits their D_2 geometrical symmetry to obtain a reduction in computational effort, accelerate statistical convergence, and improve the interpretability of results. We decompose the three-dimensional snapshots into four symmetry components. For each symmetry component, we independently perform SPOD on one quadrant of the domain. We demonstrate an application of this D_2-symmetric SPOD workflow on a large-eddy simulation of a twin-rectangular supersonic jet. Our analysis indicates that the twin jet exhibits screech at Strouhal number 0.3, and that this screech is dominated by components which are antisymmetric along the minor axis. These observations are consistent with the results from companion experiments at Ohio State University. Furthermore, the same workflow is used to analyze the symmetry-dependence of far-field acoustics at low and high frequencies.

Nomenclature

$\mathbf{C}$	=	cross-spectral density matrix
c	=	speed of sound
D_e	=	equivalent nozzle diameter $1.6h$
D_n	=	dihedral group with n mirror symmetries
h	=	nozzle height
M	=	Mach number
$N_{(\cdot)}$	=	number of $(\cdot)$
p	=	pressure
$\mathbf{Q}$	=	data matrix
$\mathbf{q}$	=	state vector
Re	=	Reynolds number
St	=	Strouhal number fD_e/U_j
T	=	temperature
t	=	time
U	=	mean streamwise velocity
u, v, w	=	Cartesian velocity components
$\mathbf{W}$	=	weight matrix
x, y, z	=	Cartesian coordinates
γ	=	adiabatic constant c_p/c_V
λ	=	SPOD eigenvalue
μ	=	dynamic viscosity
$\boldsymbol{\phi}$	=	SPOD eigenvector

*Ph.D. Student, Department of Mechanical and Aerospace Engineering, Student Member AIAA.
†Assistant Professor, Department of Mechanical and Aerospace Engineering, Senior Member AIAA.
‡Director of Operations; Senior Research Scientist - Aeroacoustics.

ρ = density

Subscript

a = acoustic property
blk = blocks
cv = control volumes
FFT = snapshots per block
j = fully-expanded nozzle exit property
max, min = maximum, minimum
ovlp = overlapping snapshots per block
s = sampling
sim = simulation
t = stagnation property
∞ = ambient property

Superscript

$(\cdot)^{\mathrm{H}}$ = Hermitian transpose
$(\cdot)^{\top}$ = transpose
$\hat{(\cdot)}$ = Fourier transform
$\bar{(\cdot)}$ = long-time mean
$(\cdot)'$ = fluctuation

I. Introduction

Spectral proper orthogonal decomposition (SPOD) is a statistical technique which has been employed in numerical studies of turbulent jets (see e.g. Towne et al. [1] and Schmidt et al. [2]). Part of the appeal of SPOD stems from its ability to educe from turbulent flows structures which are temporally as well as spatially coherent [2]. Recent applications of SPOD include the identification of Kelvin-Helmholtz (KH) type wavepackets within jet shear layers [2], and the examination of far-field acoustic radiation from jets [3].

To date, the SPOD analysis of turbulent jets has been dominated by axisymmetric configurations. Their axisymmetry can be exploited by performing a Fourier decomposition of the three-dimensional flow fields into two-dimensional azimuthal wavenumber components: a significant simplification. Non-axisymmetric jets, in contrast, cannot be azimuthally decomposed. SPOD of the large data set of a non-axisymmetric jet containing three-dimensional snapshots is thus computationally challenging and—to our knowledge—has not been demonstrated. Although they lack axisymmetry, rectangular, elliptic, and twin jets each possess two reflection symmetries: one about the major axis, another about the minor axis. It is natural to consider whether the same benefits of symmetry decomposition can be extended to these nozzle geometries as well. In this paper we present an SPOD workflow that respects the two mirror symmetries, and decomposes the three-dimensional jet flow into symmetry components.

We demonstrate this workflow on a time-resolved database collected from large-eddy simulation (LES) of the supersonic twin-rectangular jet experimentally investigated by Esfahani et al. [4] at Ohio State University (OSU). Their results have shown that the jet emits screech at the experimentally-determined, nominally ideally-expanded condition. This same condition is matched by our LES. The earliest model for screech in imperfecty expanded supersonic jets dates back to Powell [5], who proposed that screech is a resonance phenomenon involving interactions between the shear layer and shocks. Though the existence of the screech feedback loop is now widely accepted, the production and nature of the waves that sustain the loop continue to be subjects of active research. In particular, whereas the downstream-propagating waves are generally accepted to be KH instabilities [6], universal consensus regarding the upstream-propagating waves that close the loop remains elusive. Powell's original model described the upstream-propagating waves as acoustic waves traveling in the free stream [5]. However, recent findings by Gojon et al. [7] and Edgington-Mitchell et al. [8] suggest the upstream-propagating component is more likely to be a neutrally-stable acoustic mode of the mean flow, which has also been identified by Towne et al. [9] in subsonic jets. A comprehensive review of screech has been provided by Edgington-Mitchell [6].

Section II.A describes our LES of the supersonic twin-rectangular jet. The details of the symmetry-enforcing SPOD workflow are discussed in Section II.B. We demonstrate this workflow on our database in Section III, then offer

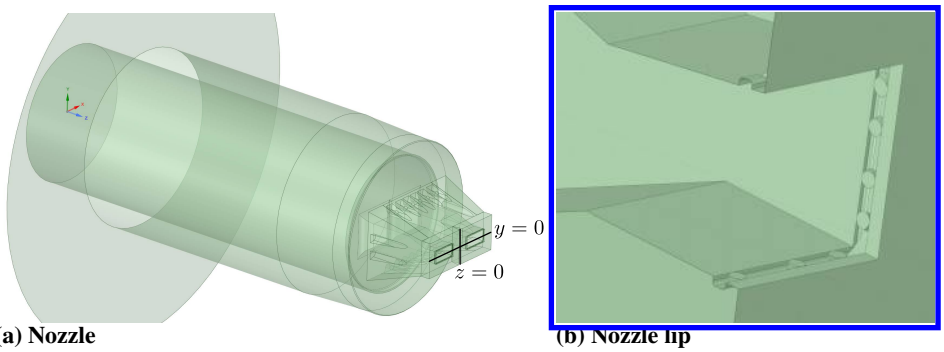

(a) Nozzle (b) Nozzle lip

Fig. 1 Twin-rectangular nozzle geometry [11], which is explicitly included in the computational domain: (a) nozzle external and internal surfaces; (b) cutaway view of the groove near the nozzle exit.

Table 1 LES parameters.

Case	M_j	M_a	Re_j	p_t/p_∞	p_j/p_∞	T_t/T_∞	T_j/T_∞	N_{cv}	$\mathrm{d}tc_\infty/h$	$t_{\text{sim}}c_\infty/h$
Baseline	1.5	1.25	1.07×10^6	3.671	1	1	0.69	77×10^6	0.002	500

concluding remarks in Section IV.

II. Numerical setup

A. Large-eddy simulation

The LES is carried out using the unstructured compressible flow solver 'Charles' [10], to simulate the twin-rectangular jet of aspect ratio two at OSU [4]. The twin-nozzle geometry is shown in Fig. 1. Fig. 1(b) highlights the nozzle lip, which includes a groove designed to house plasma actuators. For more details on the OSU facility, we refer the reader to Esfahani et al. [4].

The jet is nominally ideally-expanded and cold, at $M_j = U_j/c_j = 1.5$ and $T_j/T_\infty = 0.69$. The density, temperature, and velocities are nondimensionalized by ρ_∞, T_∞, and $c_\infty = \sqrt{\gamma p_\infty/\rho_\infty}$, respectively. Lengths are nondimensionalized by h, giving $D_e/h = 1.6$. The simulation Reynolds number, $Re_j = \rho_j U_j D_e/\mu_j = 1.07 \times 10^6$, approximately matches the OSU experiments. The nozzle pressure ratio (NPR) and nozzle temperature ratio (NTR) are $p_t/p_\infty = 3.671$ and $T_t/T_\infty = 1$, respectively. An LES of this setup was recently performed by Brès et al. [11] and validated against experimental data from OSU. To demonstrate the symmetry-enforcing SPOD workflow, we carry out an LES to collect a time-resolved flow database. Table 1 summarizes the simulation parameters.

Figure 2 visualizes the magnitude of the gradient of the instantaneous density, $|\nabla\rho|$. Fig. 2(a) is taken from the $z = 1.8h$ plane, which intersects the center line of a single nozzle; the major-axis view in Fig. 2(b) is taken from the $y = 0$ plane, which intersects the center lines of both nozzles. Although the jets are nominally ideally-expanded at the experimentally-determined design Mach number, $M_j = 1.5$, the rectangular nozzles, sharp throats, and the groove immediately upstream of each exit lead to shock cells that are visible within the potential cores.

B. Three-dimensional, D_2-symmetric SPOD

Unlike an axisymmetric jet, a twin-rectangular jet does not enjoy azimuthal symmetry; as such, its three-dimensional flow field cannot be Fourier decomposed into two-dimensional flow fields, each with a different azimuthal wavenumber. It does, however, belong in the dihedral group D_2, i.e., its geometry is invariant under reflection about the y- and z-axes. By accounting for these mirror symmetries, we propose a D_2 symmetry decomposition. Other common D_2 nozzle geometries include twin-round, single rectangular, and elliptic jets, to all of which the procedure below directly generalizes.

For the twin-rectangular jet, D_2 geometrical symmetry permits a total of four symmetric and antisymmetric components [12], which the flow must recover in a statistical sense. To describe these symmetry components

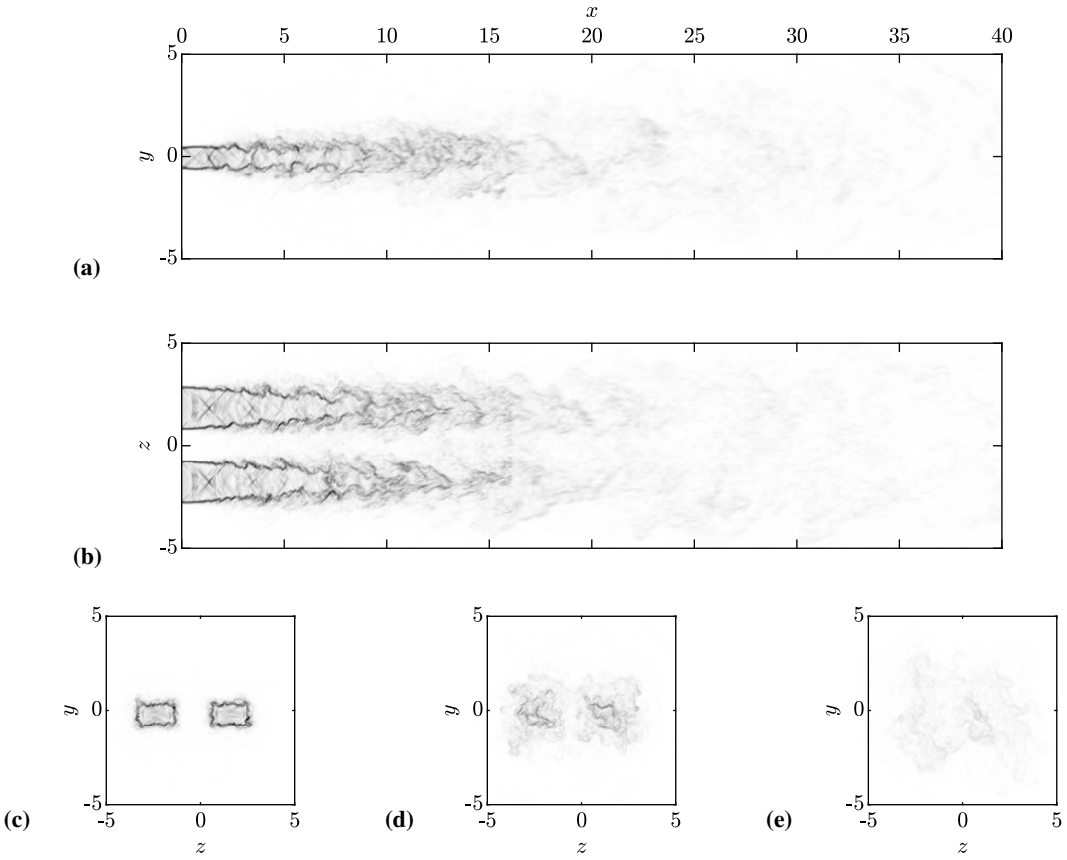

Fig. 2 Numerical schlieren (■ $0 \le |\nabla\rho| \le 6$): (a) $z = 1.8h$ plane through the center line of a single nozzle; (b) $y = 0$ plane through the center lines of both nozzles; (c–e) transverse planes through $x = 2h$, $x = 10h$, and $x = 20h$, respectively.

unambiguously, we adopt the nomenclature proposed by Rodríguez et al. [13] and subsequently used for single rectangular jets [14] as well as twin-round jets [15, 16]. Each symmetry component is denoted by two letters: SS, SA, AS, or AA. The first letter indicates symmetry (S) or antisymmetry (A) about $y = 0$; the second indicates symmetry (S) or antisymmetry (A) about $z = 0$ (see Fig. 1(a)).

To compute the D_2-symmetric SPOD, we first compute the long-time mean, $\overline{\mathbf{q}}$. Exploiting D_2 symmetry, we enforce SS symmetry on the estimated mean by averaging its four quadrants,

$$\overline{\mathbf{q}}_{\mathrm{SS}}(x,y,z) = \frac{1}{4}\begin{bmatrix} \overline{\rho}(x,y,z) + \overline{\rho}(x,-y,z) + \overline{\rho}(x,y,-z) + \overline{\rho}(x,-y,-z) \\ \overline{u}(x,y,z) + \overline{u}(x,-y,z) + \overline{u}(x,y,-z) + \overline{u}(x,-y,-z) \\ \overline{v}(x,y,z) - \overline{v}(x,-y,z) + \overline{v}(x,y,-z) - \overline{v}(x,-y,-z) \\ \overline{w}(x,y,z) + \overline{w}(x,-y,z) - \overline{w}(x,y,-z) - \overline{w}(x,-y,-z) \\ \overline{T}(x,y,z) + \overline{T}(x,-y,z) + \overline{T}(x,y,-z) + \overline{T}(x,-y,-z) \end{bmatrix}. \tag{1}$$

Note the sign changes in the $\overline{v}$ and $\overline{w}$ components. If $\overline{v}$ is symmetric about $y = 0$, then $\overline{v}(x,y,z) = -\overline{v}(x,-y,z)$; similarly, if $\overline{w}$ is symmetric about $z = 0$, then $\overline{w}(x,y,z) = -\overline{w}(x,y,-z)$. Using the improved estimate of the mean, we apply the Reynolds decomposition to the instantaneous flow field to obtain the fluctuations,

$$\mathbf{q}'(x,y,z,t) = \mathbf{q}(x,y,z,t) - \overline{\mathbf{q}}_{\mathrm{SS}}(x,y,z)\,. \tag{2}$$

Next we enforce D_2 symmetry, and decompose $\mathbf{q}'$ into four symmetry components:

$$\mathbf{q}'_{\mathrm{SS}}(x,y,z,t) = \frac{1}{4}\begin{bmatrix} \rho'(x,y,z,t) + \rho'(x,-y,z,t) + \rho'(x,y,-z,t) + \rho'(x,-y,-z,t) \\ u'(x,y,z,t) + u'(x,-y,z,t) + u'(x,y,-z,t) + u'(x,-y,-z,t) \\ v'(x,y,z,t) - v'(x,-y,z,t) + v'(x,y,-z,t) - v'(x,-y,-z,t) \\ w'(x,y,z,t) + w'(x,-y,z,t) - w'(x,y,-z,t) - w'(x,-y,-z,t) \\ T'(x,y,z,t) + T'(x,-y,z,t) + T'(x,y,-z,t) + T'(x,-y,-z,t) \end{bmatrix}, \tag{3}$$

$$\mathbf{q}'_{\mathrm{SA}}(x,y,z,t) = \frac{1}{4}\begin{bmatrix} \rho'(x,y,z,t) + \rho'(x,-y,z,t) - \rho'(x,y,-z,t) - \rho'(x,-y,-z,t) \\ u'(x,y,z,t) + u'(x,-y,z,t) - u'(x,y,-z,t) - u'(x,-y,-z,t) \\ v'(x,y,z,t) - v'(x,-y,z,t) - v'(x,y,-z,t) + v'(x,-y,-z,t) \\ w'(x,y,z,t) + w'(x,-y,z,t) + w'(x,y,-z,t) + w'(x,-y,-z,t) \\ T'(x,y,z,t) + T'(x,-y,z,t) - T'(x,y,-z,t) - T'(x,-y,-z,t) \end{bmatrix}, \tag{4}$$

$$\mathbf{q}'_{\mathrm{AS}}(x,y,z,t) = \frac{1}{4}\begin{bmatrix} \rho'(x,y,z,t) - \rho'(x,-y,z,t) + \rho'(x,y,-z,t) - \rho'(x,-y,-z,t) \\ u'(x,y,z,t) - u'(x,-y,z,t) + u'(x,y,-z,t) - u'(x,-y,-z,t) \\ v'(x,y,z,t) + v'(x,-y,z,t) + v'(x,y,-z,t) + v'(x,-y,-z,t) \\ w'(x,y,z,t) - w'(x,-y,z,t) - w'(x,y,-z,t) + w'(x,-y,-z,t) \\ T'(x,y,z,t) - T'(x,-y,z,t) + T'(x,y,-z,t) - T'(x,-y,-z,t) \end{bmatrix}, \tag{5}$$

and

$$\mathbf{q}'_{\mathrm{AA}}(x,y,z,t) = \frac{1}{4}\begin{bmatrix} \rho'(x,y,z,t) - \rho'(x,-y,z,t) - \rho'(x,y,-z,t) + \rho'(x,-y,-z,t) \\ u'(x,y,z,t) - u'(x,-y,z,t) - u'(x,y,-z,t) + u'(x,-y,-z,t) \\ v'(x,y,z,t) + v'(x,-y,z,t) - v'(x,y,-z,t) - v'(x,-y,-z,t) \\ w'(x,y,z,t) - w'(x,-y,z,t) + w'(x,y,-z,t) - w'(x,-y,-z,t) \\ T'(x,y,z,t) - T'(x,-y,z,t) - T'(x,y,-z,t) + T'(x,-y,-z,t) \end{bmatrix}. \tag{6}$$

This decomposition is analogous to the Fourier decomposition of a round jet, which belongs in the orthogonal group $O(2)$, into azimuthal wavenumber components. Like azimuthal Fourier modes, D_2 symmetry components are mutually orthogonal. As an example, by linearity of inner products,

$$\begin{aligned} \langle \mathbf{q}'_{\mathrm{SS}}(x,y,z,t), \mathbf{q}'_{\mathrm{SA}}(x,y,z,t) \rangle = {} & \langle \mathbf{q}'_{\mathrm{SS}}(x,y,z>0,t), \mathbf{q}'_{\mathrm{SA}}(x,y,z>0,t) \rangle \\ & + \langle \mathbf{q}'_{\mathrm{SS}}(x,y,z<0,t), \mathbf{q}'_{\mathrm{SA}}(x,y,z<0,t) \rangle , \end{aligned} \tag{7}$$

where we have used the fact that $\mathbf{q}'_{\mathrm{SA}}(x,y,0,t) = 0$ due to antisymmetry. Recognizing that

$$\mathbf{q}'_{\mathrm{SS}}(x,y,z<0,t) = \mathbf{q}'_{\mathrm{SS}}(x,y,z>0,t) \quad \text{and} \quad \mathbf{q}'_{\mathrm{SA}}(x,y,z<0,t) = -\mathbf{q}'_{\mathrm{SA}}(x,y,z>0,t) , \tag{8}$$

we get

$$\langle \mathbf{q}'_{\mathrm{SS}}(x,y,z,t), \mathbf{q}'_{\mathrm{SA}}(x,y,z,t) \rangle = 0 . \tag{9}$$

Therefore $\mathbf{q}'_{\mathrm{SS}}$ and $\mathbf{q}'_{\mathrm{SA}}$ are orthogonal, and the same can be shown for any pair of components. Furthermore, D_2 decomposition permits the exact reconstruction of the original flow field, $\mathbf{q}'$, by summing the four components,

$$\mathbf{q}'(x,y,z,t) = \mathbf{q}'_{\mathrm{SS}}(x,y,z,t) + \mathbf{q}'_{\mathrm{SA}}(x,y,z,t) + \mathbf{q}'_{\mathrm{AS}}(x,y,z,t) + \mathbf{q}'_{\mathrm{AA}}(x,y,z,t) , \tag{10}$$

with *no loss of generality*. In each component, all four quadrants now contain the same information. As we seek structures which are coherent over the *three*-dimensional domain, having to process just one quadrant leads to substantial memory savings for the SPOD algorithm, or indeed for any modal decomposition technique. More importantly, explicitly imposing symmetry on the fluctuations significantly accelerates the convergence of the SPOD; we will elaborate on this point in Section III.

Without loss of generality, we proceed to perform SPOD on each symmetry component independently. For each component, after taking the temporal Fourier transform of the first quadrant, at each frequency we construct the data matrix,

$$\hat{\mathbf{Q}} = \begin{bmatrix} \hat{\mathbf{q}}'^{(1)} & \hat{\mathbf{q}}'^{(2)} & \cdots & \hat{\mathbf{q}}'^{(N_{\mathrm{blk}})} \end{bmatrix}. \tag{11}$$

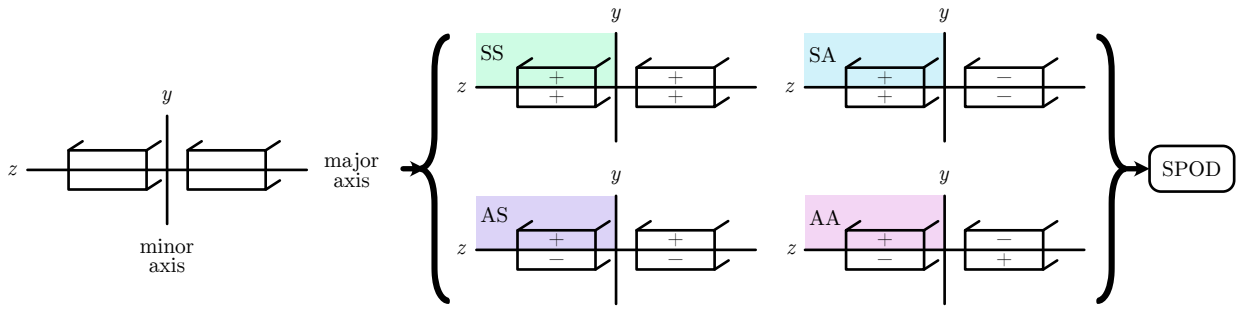

Fig. 3 Schematic of the D_2-symmetric SPOD workflow, which enforces D_2 symmetry, both minimizing memory requirement and accelerating statistical convergence.

Table 2 Interpolation and SPOD parameters.

	Database								Parameters		
Case	N_x	N_y	N_z	$[x_{\min}, x_{\max}]$	$[y_{\min}, y_{\max}]$	$[z_{\min}, z_{\max}]$	N_t	St_s	N_{FFT}	N_{ovlp}	N_{blk}
Baseline	469	202	254	$[0, 85h]$	$[-16h, 16h]$	$[-16h, 16h]$	5000	12.8	256	128	38

The eigenvalue decomposition of the cross-spectral density (CSD) matrix,

$$\hat{\mathbf{C}} = \frac{1}{N_{\text{blk}} - 1} \hat{\mathbf{Q}} \hat{\mathbf{Q}}^{\text{H}}, \tag{12}$$

is the SPOD. The weighted eigenvectors and eigenvalues of the CSD correspond to the SPOD modes and energies, respectively. In practice, we compute a smaller eigenvalue decomposition using the method of snapshots [17]. The weight matrix, $\mathbf{W}$, allows the inner product, $\langle \mathbf{q}_1, \mathbf{q}_2 \rangle = \mathbf{q}_1^{\text{H}} \mathbf{W} \mathbf{q}_2$, and by extension the eigenvalues, to be physically interpreted as mode energies. Two choices of weights will be used in this work. For $\mathbf{q}' = p'(x, y, z, t)$, we choose

$$\mathbf{W} = \int_0^{z_{\max}} \int_0^{y_{\max}} \int_{x_{\min}}^{x_{\max}} \mathrm{d}x \, \mathrm{d}y \, \mathrm{d}z \,, \tag{13}$$

such that the SPOD eigenvalues represent the volume-integrated variance of the pressure fluctuations; for $\mathbf{q}' = [\rho, u, v, w, T]^{\top}(x, y, z, t)$, we choose

$$\mathbf{W} = \int_0^{z_{\max}} \int_0^{y_{\max}} \int_{x_{\min}}^{x_{\max}} \mathrm{diag}\left(\frac{\overline{T}}{\gamma \overline{\rho} M_j^2}, \overline{\rho}, \overline{\rho}, \overline{\rho}, \frac{\overline{\rho}}{\gamma(\gamma - 1)\overline{T} M_j^2} \right) \mathrm{d}x \, \mathrm{d}y \, \mathrm{d}z \,, \tag{14}$$

such that the eigenvalues represent the volume-integrated compressible energy density [18].

The D_2-symmetric SPOD workflow is illustrated in Fig. 3. For an in-depth discussion of the SPOD algorithm itself, we direct the reader to Schmidt and Colonius [19].

III. Results

To perform D_2-symmetric SPOD, the unstructured LES data are first interpolated onto a Cartesian grid; the interpolation parameters are summarized in Table 2. The data are then Reynolds- and D_2-decomposed according to Eqs. (2) and (10), respectively. To exemplify D_2 decomposition, Fig. 4 shows representative snapshots of the SS, SA, AS, and AA components of the instantaneous streamwise velocity fluctuations, u'. In Fig. 4(a,c,e,f), for instance, u'_{SS} is symmetric about both $y = 0$ and $z = 0$. By analogy, u'_{SA}, u'_{AS}, and u'_{AA} are symmetric or antisymmetric about $y = 0$ or $z = 0$. For each symmetry component, we independently compute the SPOD using the parameters listed in Table 2. The eigenvalue spectra from the SPOD of the pressure are shown in Fig. 5(b–e). The blue curves represent the volume-integrated power spectral densities (PSD), reconstructed by summing all the eigenvalues at each

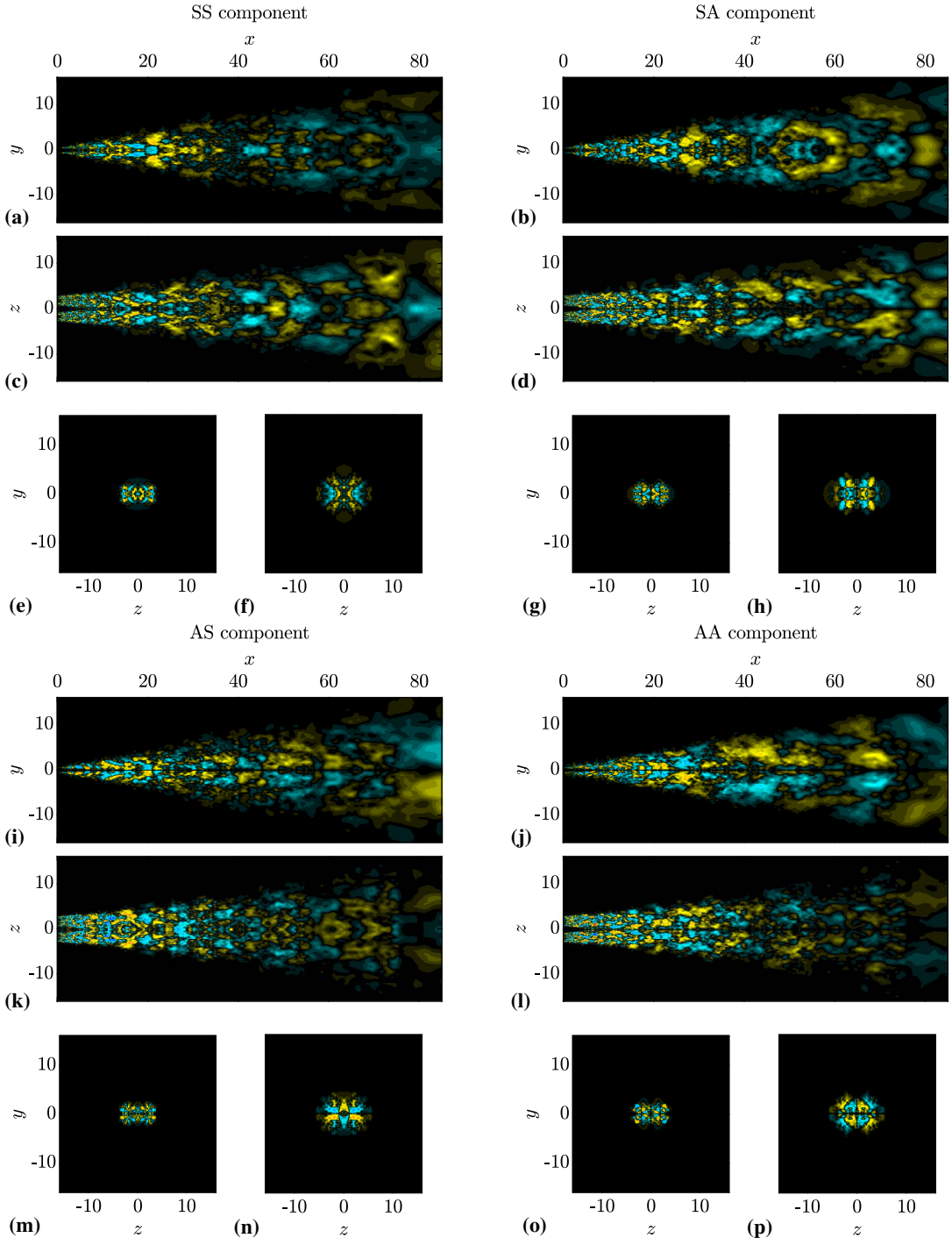

Fig. 4 Symmetry-decomposed instantaneous streamwise velocity fluctuations: (a,c,e,f) SS component (+ +; + +; $-0.47 \le u'_{SS} \le 0.47$); (b,d,g,h) SA component (+ −; + −; $-0.38 \le u'_{SA} \le 0.38$); (i,k,m,n) AS component (− +; − +; $-0.37 \le u'_{AS} \le 0.37$); (j,l,o,p) AA component (− −; + +; $-0.38 \le u'_{AA} \le 0.38$). (a,b,i,j) show the $z = 1.8h$ plane through the center line of a single nozzle; (c,d,k,l) show the $y = 0.5h$ plane through the lip lines of both nozzles; (e,g,m,o) show the $x = 10h$ plane; (f,h,n,p) show the $x = 20h$ plane.

frequency. Highlighted in red are the separations between the leading and first suboptimal eigenvalues. In the AA and AS components (Fig. 5(b,c)), there is a distinct peak at $St = 0.3$. At this frequency, the large separation brought about by the peak in turn indicates the dominance of a physical instability [2], in this case the screech tone [4, 11]. The absence of this low-rank behavior from the SS or SA components (Fig. 5(d,e)) suggests the AA and AS components are primarily responsible for screech.

For comparison only, we also compute the SPOD of the pressure over the entire flow field, without D_2 decomposition. The resulting spectra are shown in Fig. 5(a). The leading and first suboptimal eigenvalues show a prominent peak at $St = 0.3$, corresponding to the peak at the same frequency in the leading eigenvalues of the AA and AS components. By energy conservation, the PSD is four times the sum of the PSDs of the individual symmetry components, which reflects the fact that SPOD of the non-D_2-decomposed data is carried out over all four quadrants, while SPOD of each symmetry component is carried out over only a single quadrant.

Given that SPOD seeks orthogonal modes, and that different symmetry components are mutually orthogonal, the SPOD of non-D_2-decomposed data must *eventually* recover all four symmetry components, *provided* the number of realizations is sufficiently large to converge them. This means that in general, given a finite sample, without D_2 decomposition there is no guarantee SPOD will recover all four symmetries. In the case of our twin jet, however, the four leading modes of the full data correspond to the leading mode of each symmetry component, with the caveat that the fourth mode cannot be unambiguously characterized due to lack of convergence. Figures 6, 7, 8, and 9 compare the four leading SPOD modes at $St = 0.3$, with (right column) and without (left column) D_2 decomposition. Recall that when D_2 symmetry is enforced, the eigenvectors need only be computed and stored in the first quadrant, i.e., $x, y, z \in [0, 85h] \times [0, 16h] \times [0, 16h]$; here these eigenvectors have been unfolded into the remaining three quadrants for visual clarity. The first, second, and third SPOD modes of the non-D_2-decomposed pressure clearly resemble the first SPOD mode of the AA, AS, and SS components, respectively. However, with D_2 decomposition, the mode shapes appear smoother, implying better statistical convergence. They are also perfectly (anti-)symmetric by construction. The fourth SPOD mode of the non-D_2-decomposed pressure is too poorly converged for visual confirmation that it is equivalent to the first SPOD mode of the SA component. Nevertheless it is noteworthy that both modes show the wavenumber has doubled in the z-direction, relative to the three preceding pairs of modes.

Figure 10 shows the eigenvalues of the SPOD of the primitive variables vector, $[\rho, u, v, w, T]^\top$, decomposed into symmetry components. As with the pressure SPOD spectra in Fig. 5, we observe a peak corresponding to the screech tone at $St = 0.3$, only in the AA and AS components, not SS or SA. For each symmetry component, the normalized pressure components of the leading SPOD modes at $St = 0.3$ and 0.9 are visualized as 3D isosurfaces of $\boldsymbol{\phi}/\|\boldsymbol{\phi}\|_\infty = \pm 0.3$ in Fig. 11. We select this isovalue, ± 0.3, to highlight the near-field hydrodynamic structures. KH-type wavepackets, previously observed in axisymmetric jets [2], are evident here in the shear layers. At higher frequency, the maximum amplitude of the modes is localized further upstream, and the modes do not extend as far downstream.

Figure 12 visualizes the 3D isosurfaces of $\boldsymbol{\phi}/\|\boldsymbol{\phi}\|_\infty = \pm 0.025$. The smaller isovalue highlights the acoustic radiation into the far field. The acoustical structures are very well-defined, and are distinctly characterized by a single wavenumber, which is consistent with the observation that the most coherent structures in the jet are the ones that most efficiently radiate sound into the far field [20]. At $St = 0.3$ (Fig. 12(a,c,e,g)), only the AA, AS, and SS components produce large acoustic perturbations. Such perturbations are much less visible in the SA component. Note that each mode is normalized with its maximum amplitude, not scaled by energy. Among the AA, AS, and SS components, SS demonstrates increasing amplitude with downstream distance, whereas the amplitudes of AA and AS decrease with downstream distance. This should come as no surprise: at $St = 0.3$, AA and AS exhibit screech (Fig. 5 and 10), which originates in the interaction between the shear layers and the shocks [6]. As the shocks weaken with downstream distance, so does the shock-associated far-field sound. At $St = 0.9$, the AA, AS, and SA components show distinct far-field acoustic fields (Fig. 12(b,d,h)), whereas the SS component does not (Fig. 12(f)).

IV. Conclusion

Geometrical symmetries in a turbulent flow give rise to symmetries in its turbulent statistics. When such symmetries exist, they should always be exploited for statistical analysis. In the SPOD framework, we exploit stationarity by taking the temporal Fourier transform. When analyzing an axisymmetric jet, we exploit azimuthal homogeneity by decomposing the flow into azimuthal wavenumber components. In this work, we extend symmetry decomposition to jets in the D_2 symmetry group, i.e., nozzle geometries that possess two planes of reflection symmetry. As a demonstration of D_2-symmetric SPOD, we carried out the LES of a Mach 1.5, nominally ideally-expanded twin-rectangular jet. We decomposed the resulting snapshots into four symmetry components, SS, SA, AS, and AA. For each component,

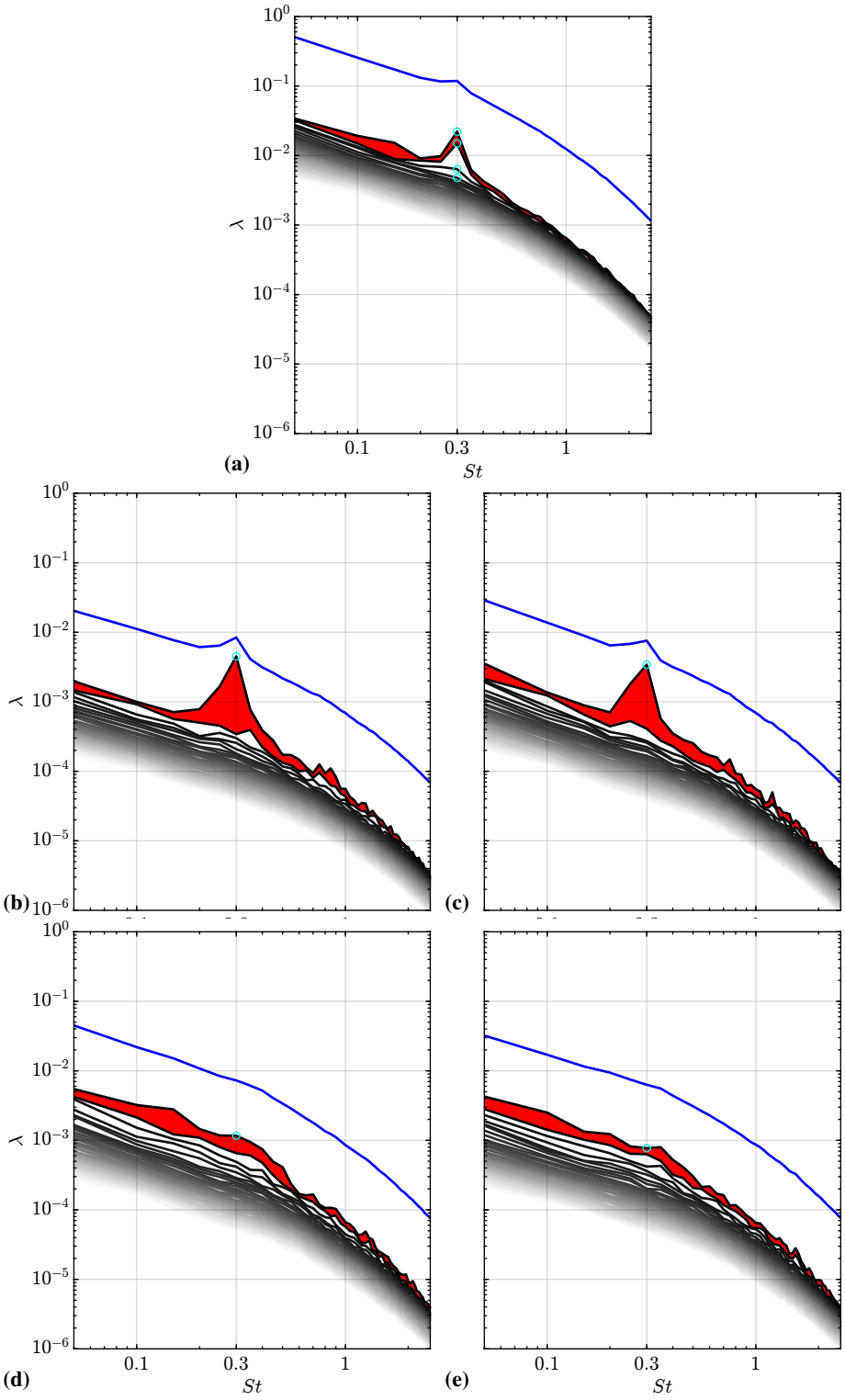

Fig. 5 Eigenvalue spectra of the SPOD of pressure: (a) non-D_2-decomposed fluctuations; (b) AA component ($^{\pm}_{+}$ $^{-}_{+}$); (c) AS component ($^{\pm}_{-}$ $^{\pm}_{+}$); (d) SS component ($^{+}_{+}$ $^{+}_{+}$); (e) SA component ($^{+}_{+}$ $^{-}_{+}$). The separation between the leading and first suboptimal eigenvalues is highlighted in red. The volume-integrated PSD, reconstructed by summing the eigenvalues at each frequency, is shown in blue. The modes marked with cyan circles are shown in Fig. 6, 7, 8, and 9.

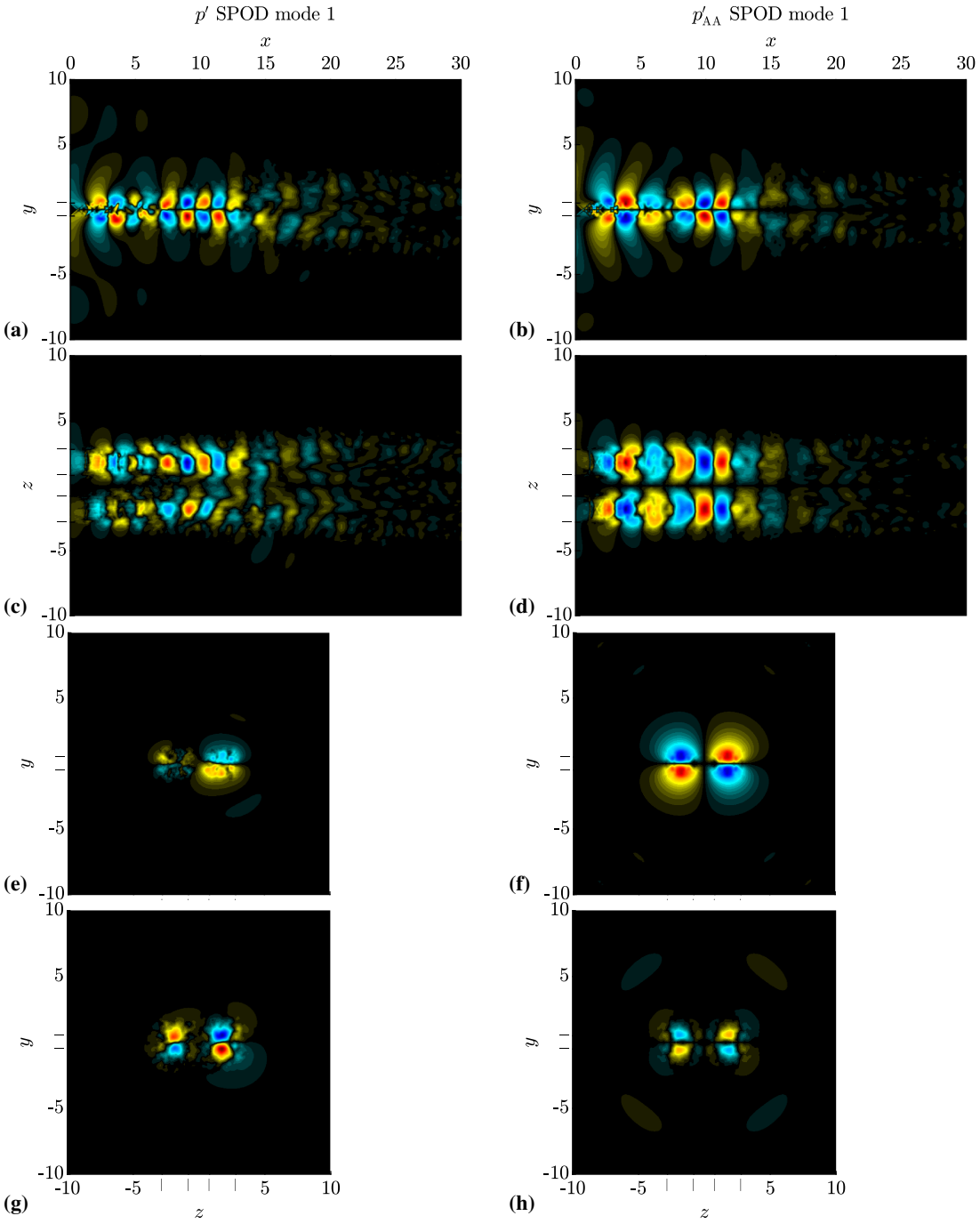

Fig. 6 Comparison between SPOD mode 1 of the non-D_2-decomposed pressure fluctuations (a,c,e,g) and SPOD mode 1 of the AA component ($^{+}_{+}$ $^{-}_{-}$) of the pressure fluctuations (b,d,f,h), at $St = 0.3$. (a,b) show the $z = 1.8h$ plane though the center line of a single nozzle; (c,d) show the $y = 0.5h$ plane through the lip lines of both nozzles; (e,f) show the $x = 4h$ plane; (g,h) show the $x = 9h$ plane. Modes have been normalized ($-1 \leq \boldsymbol{\phi}/\|\boldsymbol{\phi}\|_\infty \leq 1$). The corresponding eigenvalues are marked with cyan circles in Fig. 5. Nozzle lip lines are marked with black lines.

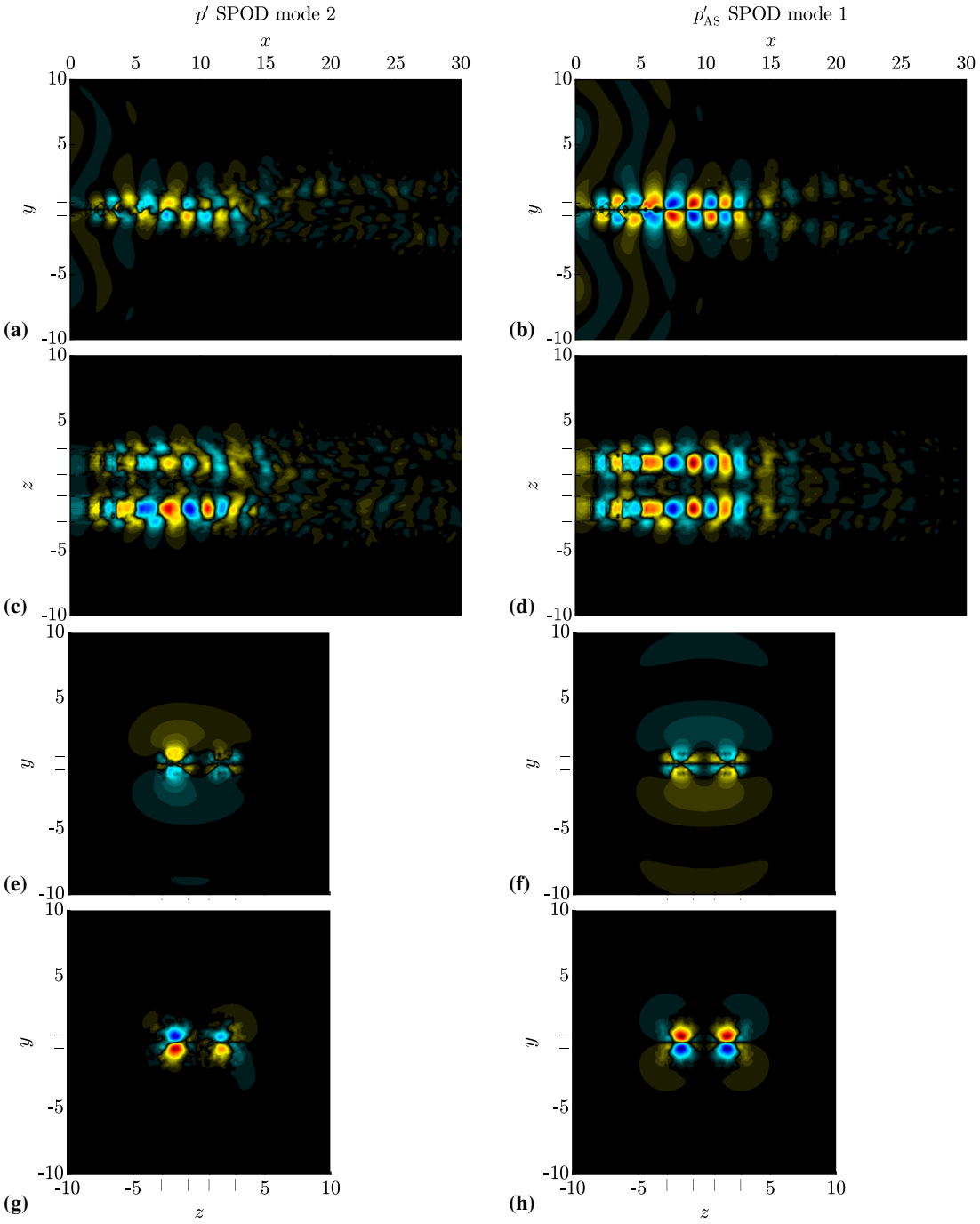

Fig. 7 Comparison between SPOD mode 2 of the non-D_2-decomposed pressure fluctuations (a,c,e,g) and SPOD mode 1 of the AS component ($\pm\ \pm$) of the pressure fluctuations (b,d,f,h), at $St = 0.3$. (a,b) show the $z = 1.8h$ plane though the center line of a single nozzle; (c,d) show the $y = 0.5h$ plane through the lip lines of both nozzles; (e,f) show the $x = 4h$ plane; (g,h) show the $x = 9h$ plane. Modes have been normalized ($-1 \leq \boldsymbol{\phi}/\|\boldsymbol{\phi}\|_\infty \leq 1$). The corresponding eigenvalues are marked with cyan circles in Fig. 5. Nozzle lip lines are marked with black lines.

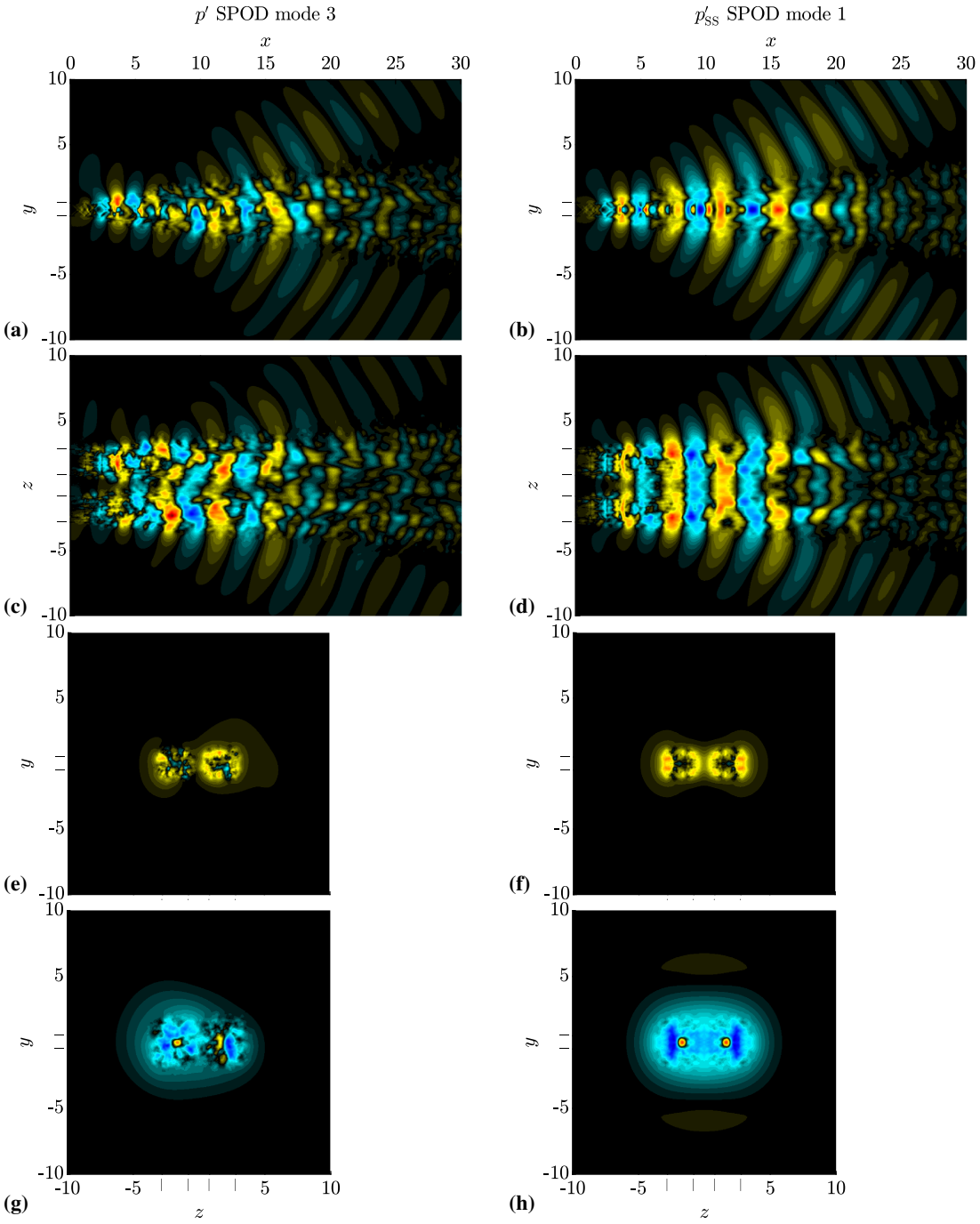

Fig. 8 Comparison between SPOD mode 3 of the non-D_2-decomposed pressure fluctuations (a,c,e,g) and SPOD mode 1 of the SS component ($^{+}_{+}$ $^{+}_{+}$) of the pressure fluctuations (b,d,f,h), at $St = 0.3$. (a,b) show the $z = 1.8h$ plane though the center line of a single nozzle; (c,d) show the $y = 0.5h$ plane through the lip lines of both nozzles; (e,f) show the $x = 4h$ plane; (g,h) show the $x = 9h$ plane. Modes have been normalized ($-1 \leq \boldsymbol{\phi}/\|\boldsymbol{\phi}\|_\infty \leq 1$). The corresponding eigenvalues are marked with cyan circles in Fig. 5. Nozzle lip lines are marked with black lines.

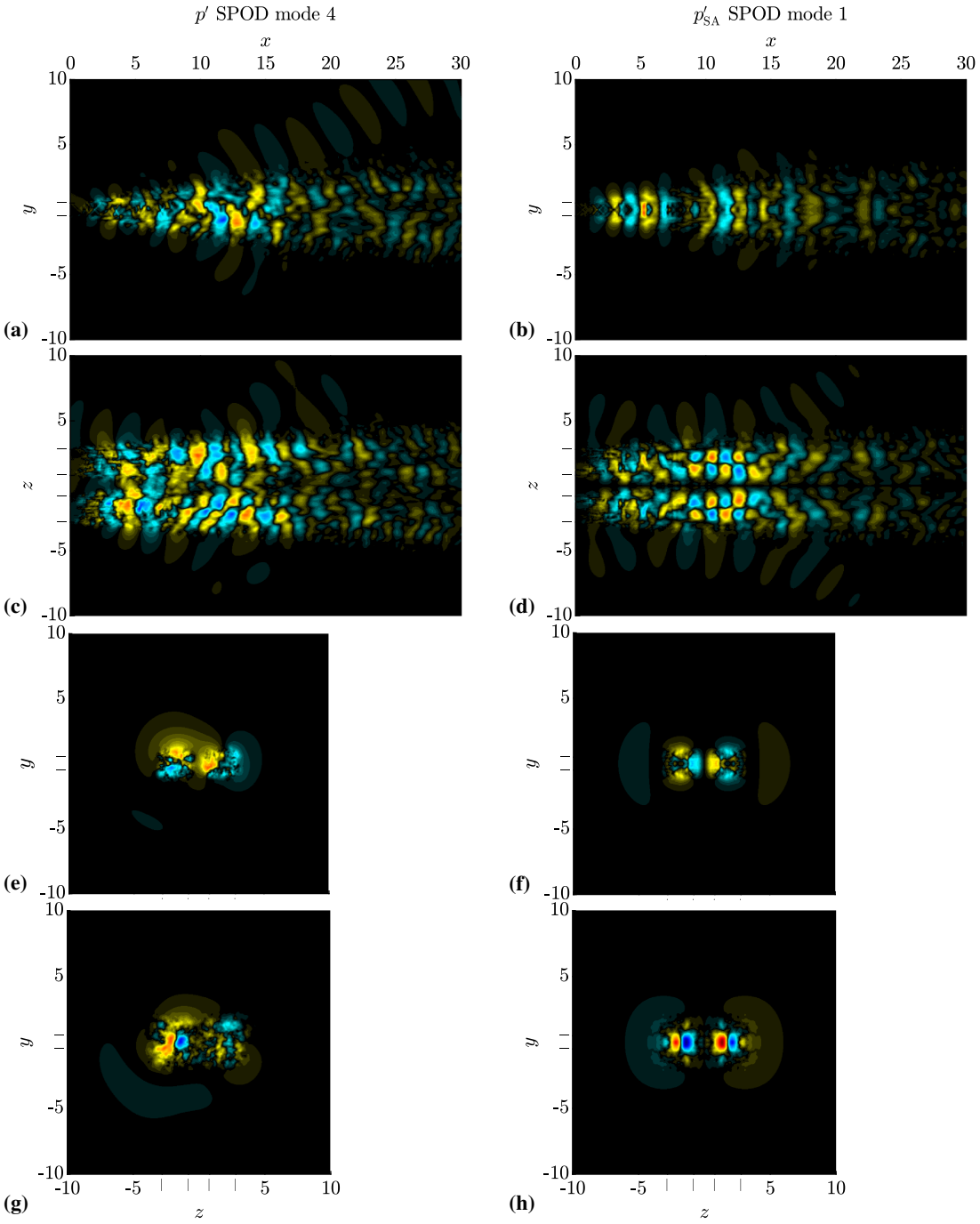

Fig. 9 Comparison between SPOD mode 4 of the non-D_2-decomposed pressure fluctuations (a,c,e,g) and SPOD mode 1 of the SA component ($^{+}_{+}$ $^{-}_{-}$) of the pressure fluctuations (b,d,f,h), at $St = 0.3$. (a,b) show the $z = 1.8h$ plane though the center line of a single nozzle; (c,d) show the $y = 0.5h$ plane through the lip lines of both nozzles; (e,f) show the $x = 4h$ plane; (g,h) show the $x = 9h$ plane. Modes have been normalized ($-1 \leq \boldsymbol{\phi}/\|\boldsymbol{\phi}\|_\infty \leq 1$). The corresponding eigenvalues are marked with cyan circles in Fig. 5. Nozzle lip lines are marked with black lines.

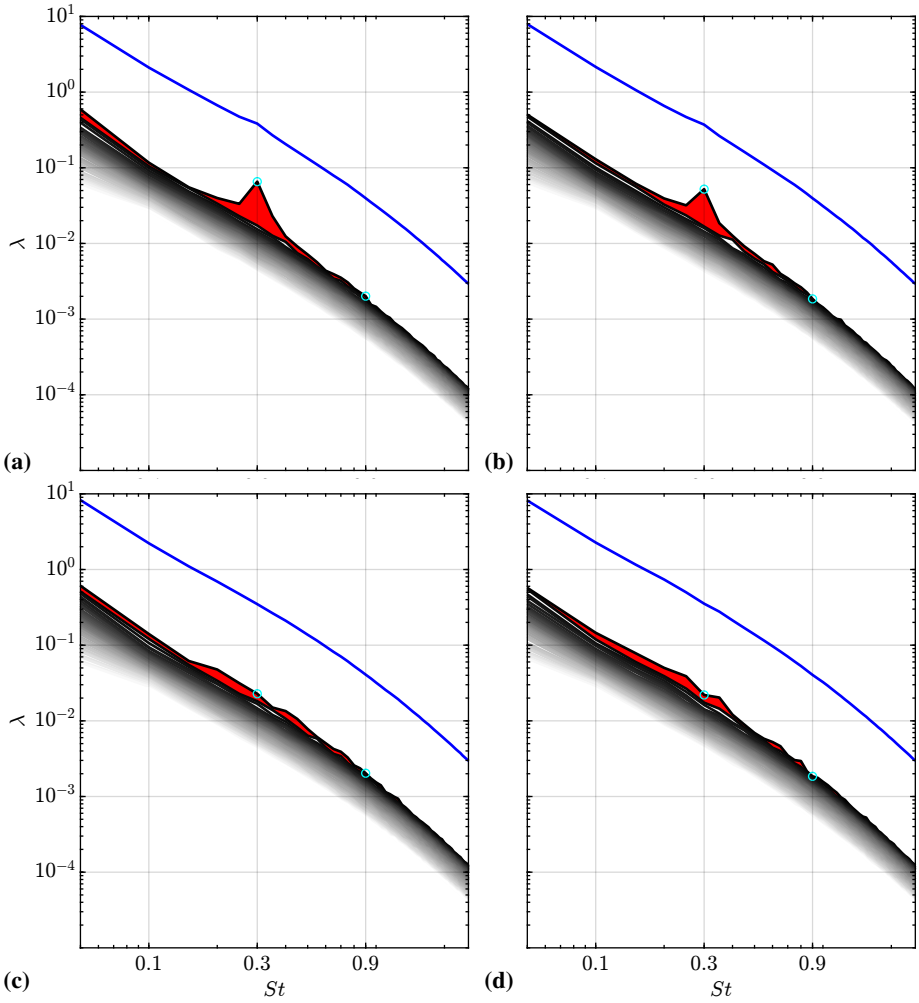

Fig. 10 Eigenvalue spectra of the SPOD of the primitive variables vector, $[\rho, u, v, w, T]^\top$: (a) AA component ($^{+}_{-}$ $^{-}_{+}$); (b) AS component ($^{+}_{-}$ $^{+}_{-}$); (c) SS component ($^{+}_{+}$ $^{+}_{+}$); (d) SA component ($^{+}_{+}$ $^{-}_{+}$). The separation between the leading and first suboptimal eigenvalues is highlighted in red. The volume-integrated PSD, reconstructed by summing the eigenvalues at each frequency, is shown in blue. The modes marked with cyan circles are shown in Fig. 11 and 12.

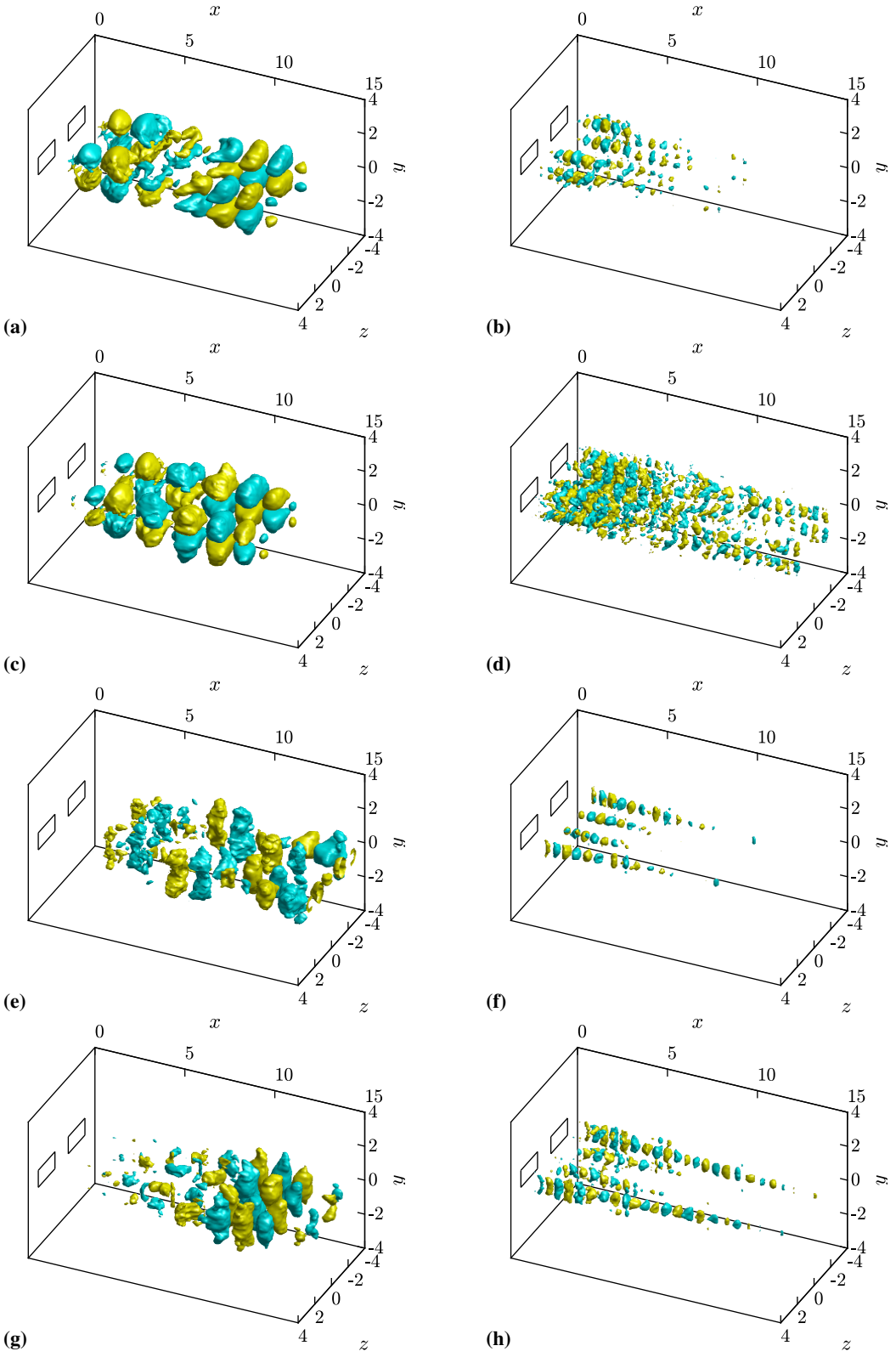

Fig. 11 The pressure components of the leading SPOD modes of the primitive variables vector, decomposed into AA (a,b), AS (c,d), SS (e,f), and SA (g,h) components, at $St = 0.3$ (a,c,e,g) and $St = 0.9$ (b,d,f,h). Isosurfaces of $\boldsymbol{\phi}/\|\boldsymbol{\phi}\|_\infty = \pm 0.3$ ( ) are shown. The corresponding eigenvalues are marked with cyan circles in Fig. 10.

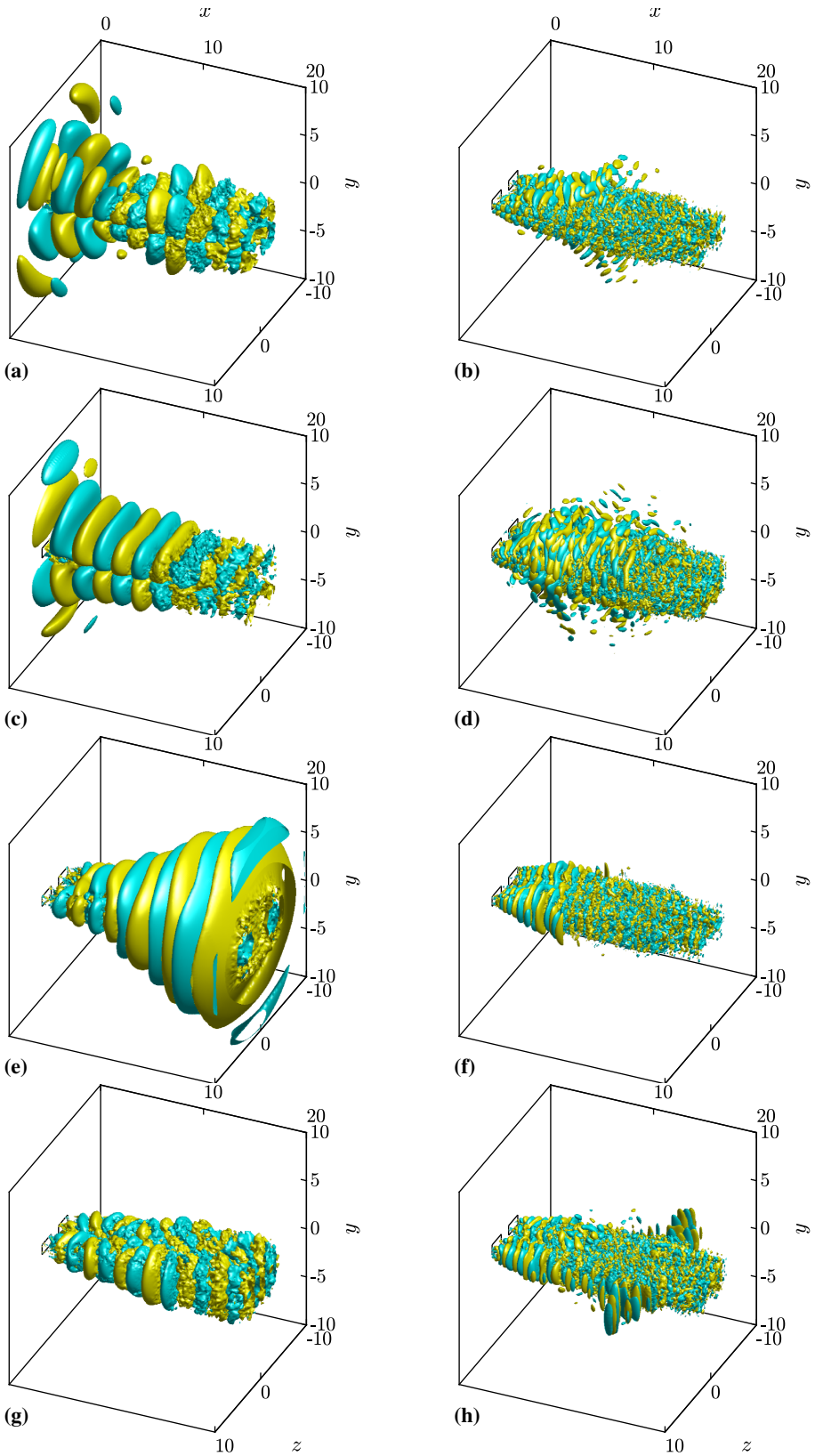

Fig. 12 The pressure components of the leading SPOD modes of the primitive variables vector, decomposed into AA (a,b), AS (c,d), SS (e,f), and SA (g,h) components, at $St = 0.3$ (a,c,e,g) and $St = 0.9$ (b,d,f,h). Isosurfaces of $\boldsymbol{\phi}/\|\boldsymbol{\phi}\|_\infty = \pm 0.025$ ( ) are shown. The corresponding eigenvalues are marked with cyan circles in Fig. 10.

we performed an independent SPOD analysis, without loss of generality. A comparison between SPOD with and without D_2 decomposition confirms that D_2 decomposition both accelerates statistical convergence and reduces memory requirement—crucial to the efficient use of high-performance computing and local post-processing resources. In terms of flow physics, the eigenvalue spectra confirm the screech tone at $St = 0.3$ observed in LES by Brès et al. [11] as well as in companion experiments by Esfahani et al. [4]. Microphone measurements from Esfahani et al. [4] also showed that the screech mode is antisymmetric along the minor axis. This is again confirmed by our analysis: D_2-symmetric SPOD identifies the AA and AS components, both of which are antisymmetric along the minor axis, as the primary sources of screech. Our SPOD, which is carried out in 3D, further suggests the screech mode can be either symmetric or antisymmetric along the major axis. 3D isosurfaces of the SPOD modes reveal the symmetry-dependence of the far-field acoustics. At low frequency, the AA, AS, and SS components produce clear acoustic structures. At higher frequency, however, AA, AS, and SA are the components that radiate well-defined acoustic fields. These observations suggest that D_2 decomposition offers more than computational convenience: it improves the interpretability of results.

The twin-rectangular jet's natural preference for the AA and AS components at the screech frequency opens up the possibility for the dominant instabilities of the jet to be controlled through external forcing. We plan to apply D_2-symmetric SPOD to the simulation of a forced, twin-rectangular jet. As part of future work, we will also apply D_2 decomposition to other modal decomposition techniques to analyze the twin jet.

Acknowledgments

We gratefully acknowledge support from Office of Naval Research award N00014-20-1-2311, under the supervision of Dr. Steve Martens. LES calculations were carried out on the "Onyx" Cray XC40/50 system in ERDC DSRC, using allocations provided by DoD HPCMP.

References

[1] Towne, A., Schmidt, O. T., and Colonius, T., "Spectral proper orthogonal decomposition and its relationship to dynamic mode decomposition and resolvent analysis," *Journal of Fluid Mechanics*, Vol. 847, 2018, pp. 821–867. https://doi.org/10.1017/jfm.2018.283.

[2] Schmidt, O. T., Towne, A., Rigas, G., Colonius, T., and Brès, G. A., "Spectral analysis of jet turbulence," *Journal of Fluid Mechanics*, Vol. 855, 2018, pp. 953–982. https://doi.org/10.1017/jfm.2018.675.

[3] Nekkanti, A., and Schmidt, O. T., "Modal Analysis of Acoustic Directivity in Turbulent Jets," *AIAA Journal*, Vol. 59, No. 1, January 2021, pp. 228–239. https://doi.org/10.2514/1.J059425.

[4] Esfahani, A., Webb, N., and Samimy, M., "Coupling Modes in Supersonic Twin Rectangular Jets," *AIAA Paper 2021–1292*, January 2021. https://doi.org/10.2514/6.2021-1292.

[5] Powell, A., "The Noise of Choked Jets," *Journal of the Acoustical Society of America*, Vol. 25, No. 3, 1953, pp. 385–389. https://doi.org/10.1121/1.1907052.

[6] Edgington-Mitchell, D., "Aeroacoustic resonance and self-excitation in screeching and impinging supersonic jets – A review," *International Journal of Aeroacoustics*, Vol. 18, No. 2–3, 2019, pp. 118–188. https://doi.org/10.1177/1475472X19834521.

[7] Gojon, R., Bogey, C., and Mihaescu, M., "Oscillation Modes in Screeching Jets," *AIAA Journal*, Vol. 56, No. 7, 2018, pp. 2918–2924. https://doi.org/10.2514/1.J056936.

[8] Edgington-Mitchell, D., Jaunet, V., Jordan, P., Towne, A., Soria, J., and Honnery, D., "Upstream-travelling acoustic jet modes as a closure mechanism for screech," *Journal of Fluid Mechanics*, Vol. 855, No. R1, 2018, pp. 1–12. https://doi.org/10.1017/jfm.2018.642.

[9] Towne, A., Cavalieri, A. V. G., Jordan, P., Colonius, T., Schmidt, O., Jaunet, V., and Brès, G. A., "Acoustic resonance in the potential core of subsonic jets," *Journal of Fluid Mechanics*, Vol. 825, 2017, pp. 1113–1152. https://doi.org/10.1017/jfm.2017.346.

[10] Brès, G. A., Ham, F. E., Nichols, J. W., and Lele, S. K., "Unstructured Large-Eddy Simulations of Supersonic Jets," *AIAA Journal*, Vol. 55, No. 4, April 2017, pp. 1164–1184. https://doi.org/10.2514/1.J055084.

[11] Brès, G. A., Yeung, B. C. Y., Schmidt, O. T., Esfahani, A., Webb, N., Samimy, M., and Colonius, T., "Towards large-eddy simulations of supersonic jets from twin rectangular nozzle with plasma actuation," *AIAA Paper 2021–2154*, August 2021. https://doi.org/10.2514/6.2021-2154.

[12] Tam, C. K. W., and Thies, A. T., "Instability of rectangular jets," *Journal of Fluid Mechanics*, Vol. 248, 1993, pp. 425–448. https://doi.org/10.1017/S0022112093000837.

[13] Rodríguez, D., Jotkar, M. R., and Gennaro, E. M., "Wavepacket models for subsonic twin jets using 3D parabolized stability equations," *Comptes Rendus Mecanique*, Vol. 346, July 2018, pp. 890–902. https://doi.org/10.1016/j.crme.2018.07.002.

[14] Rodríguez, D., Prasad, C., and Gaitonde, D., "Near-field turbulent structures in supersonic rectangular jets using 3D parabolized stability equations," *AIAA paper 2021–2276*, August 2021. https://doi.org/10.2514/6.2021-2276.

[15] Rodríguez, D., "Wavepacket models for supersonic twin-jets," *AIAA paper 2021–2121*, August 2021. https://doi.org/10.2514/6.2021-2121.

[16] Stavropoulos, M. N., Mancinelli, M., Jordan, P., Jaunet, V., Edgington-Mitchell, D. M., and Nogueira, P. A. S., "Understanding twin-jet screech using a vortex-sheet model," *AIAA paper 2021–2249*, August 2021. https://doi.org/10.2514/6.2021-2249.

[17] Sirovich, L., "Turbulence and the Dynamics of Coherent Structures Part I: Coherent Structures," *Quarterly of Applied Mathematics*, Vol. 45, No. 3, 1987, pp. 561–571. https://doi.org/10.1090/qam/1987-45-03.

[18] Chu, B.-T., "On the Energy Transfer to Small Disturbances in Fluid Flow (Part I)," *Acta Mechanica*, Vol. 1, September 1965, pp. 215–234. https://doi.org/10.1007/BF01387235.

[19] Schmidt, O. T., and Colonius, T., "Guide to Spectral Proper Orthogonal Decomposition," *AIAA Journal*, Vol. 58, No. 3, 2020, pp. 1023–1033. https://doi.org/10.2514/1.J058809.

[20] Jordan, P., and Colonius, T., "Wave Packets and Turbulent Jet Noise," *Annual Review of Fluid Mechanics*, Vol. 45, 2013, pp. 173–195. https://doi.org/10.1146/annurev-fluid-011212-140756.